

Zimmerli, Allegretti et al

1 Nuclear pores constrict upon energy 2 depletion

3
4
5 Christian E. Zimmerli*^{1,2,5}, Matteo Allegretti*¹, Vasileios Rantos^{3,4}, Sara K. Goetz^{1,2}, Agnieszka
6 Obarska-Kosinska^{4,6}, Ievgeniia Zagoriy¹, Aliaksandr Halavatyi⁵, Julia Mahamid¹, Jan
7 Kosinski^{1,3,4} and Martin Beck^{1,6}

8
9 * Contributed equally
10
11 Correspondence to jan.kosinski@embl.de or martin.beck@biophys.mpg.de
12

13 Affiliations:

14 1 Structural and Computational Biology Unit, European Molecular Biology Laboratory,
15 Meyerhofstraße 1, 69117, Heidelberg, Germany

16 2 Collaboration for joint PhD degree between EMBL and Heidelberg University, Faculty of
17 Biosciences

18 3 Centre for Structural Systems Biology (CSSB), Notkestraße 85, 22607, Hamburg, Germany

19 4 European Molecular Biology Laboratory Hamburg, Notkestraße 85, 22607, Hamburg,
20 Germany

21 5 Advanced Light Microscopy Facility, European Molecular Biology Laboratory,
22 Meyerhofstraße 1, 69117, Heidelberg, Germany

23 6 Department of Molecular Sociology, Max Planck Institute of Biophysics, Max-von-Laue-
24 Straße 3, 60438 Frankfurt am Main

25
26 **Keywords:** nuclear pore complex, cryo-FIB milling, cryo-electron tomography, nuclear
27 transport

28

Zimmerli, Allegretti et al

29 **Abstract**

30 Nuclear pore complexes (NPCs) fuse the inner and outer nuclear membranes and mediate
31 nucleocytoplasmic exchange. They are made of 30 different nucleoporins that form an
32 intricate cylindrical architecture around an aqueous central channel. This architecture is
33 highly dynamic in space and time. Variations in NPC diameter were reported, but the
34 physiological circumstances and the molecular details remain unknown. Here we combined
35 cryo-electron tomography and subtomogram averaging with integrative structural modeling
36 to capture a molecular movie of the respective large-scale conformational changes *in cellulo*.
37 While actively transporting NPCs adopt a dilated conformation, they strongly constrict upon
38 cellular energy depletion. Fluorescence recovery after photo bleaching experiments show
39 that NPC constriction is concomitant with reduced diffusion and active transport across the
40 nuclear envelope. Our data point to a model where the energy status of cells is linked to the
41 conformation of NPC architecture.

42 **Introduction**

43 Nuclear pore complexes (NPCs) bridge the nuclear envelope (NE) and facilitate
44 nucleocytoplasmic transport. Across the eukaryotic kingdom, about 30 different genes
45 encode for NPC components, termed nucleoporins (Nups). Although specialized Nups have
46 been identified in many species, extensive biochemical and structural studies *in vitro* led to
47 the consensus that the core scaffold inventory is conserved. It consists of several Nup
48 subcomplexes that come together in multiple copies to form an assembly of eight asymmetric
49 units, called spokes, that are arranged in a rotationally symmetric fashion (1). The Y-complex
50 (also called Nup107 complex) is the major component of the outer rings (the nuclear and
51 cytoplasmic rings; NR and CR), which are placed distally into the nuclear and cytoplasmic
52 compartments. The inner ring complex scaffolds the inner ring (IR; also called spoke ring) that
53 resides at the fusion plane of the nuclear membranes. The Nup159 complex (also called P-
54 complex) asymmetrically associates with the Y-complex of the cytoplasmic ring and mediates
55 mRNA export. Despite these common features of quaternary structure, *in situ* structural
56 biology studies have revealed that the higher order assembly is variable across the eukaryotic
57 kingdom (2).

58

59 In addition to compositional variability across different species, NPC architecture is
60 conformationally highly dynamic and variations in NPC diameter have been observed in
61 various species and using different methods (3–7). It has been shown that dilation is part of
62 the NPC assembly process (8, 9). However, if NPC dilation and constriction may play a role
63 during active nuclear transport (10), or are required to open up peripheral channels for the
64 import of inner nuclear membrane proteins (11–13), remains controversial. It is difficult to
65 conceive that such large-scale conformational changes can occur on similar time scales as
66 individual transport events (14, 15), which would be the essence of a physical gate.
67 Nevertheless, several cues that potentially could affect NPC diameter have been suggested,
68 such as exposure to mechanical NE stress, mutated forms of Importin β , varying Ca^{2+}
69 concentrations or hexanediol (7, 16–21). However, these previous studies did neither explore
70 NPC diameter and its functional consequences within intact cellular environments nor did
71 they structurally analyze the conformational changes of nuclear pores in molecular detail.
72 Thus, physiological cause and consequence along with the molecular mechanisms of NPC
73 dilation and constriction remain enigmatic.

Zimmerli, Allegretti et al

74
75 Active nuclear transport of cargo relies on energy supply. Importin or exportin-mediated
76 transport requires the small GTPase RAN that binds either GTP in the nucleus or GDP in the
77 cytoplasm to ensure directionality of transport (22), while mRNA export is directly ATP
78 dependent (23). Cells of various organisms including *Schizosaccharomyces pombe* show a
79 rapid shut down of active nuclear transport and mRNA export when depleted of ATP (24–26).
80 This points to a well conserved mechanism, likely dependent on a concomitantly reduced
81 availability of free GTP (27). Moreover, energy depletion (ED) leads to a general
82 reorganization of the cytoplasm including solidification of the periplasm, general water loss
83 and reduction of the nuclear and cellular volume, which allows cells to endure under
84 unfavorable conditions (28–31). If the shutdown of active nuclear transport coincides with
85 the alteration in passive diffusion and potentially a conformational adaption of NPC
86 architecture remains unknown.

87
88 Here we demonstrate that in *S. pombe* NPCs (SpNPCs) constrict under conditions of ED, which
89 is concomitant with a reduction of both, free diffusion and active nuclear transport across the
90 nuclear envelope. Using *in cellulo* cryo-electron microscopy (cryo-EM) and integrative
91 structural modeling, we captured a molecular movie of NPC constriction. Our dynamic
92 structural model suggests large scale conformational changes that occur by movements of
93 the spokes with respect to each other but largely preserve the arrangement of individual
94 subcomplexes. Previous structural models obtained from isolated nuclear envelopes (32–37)
95 thereby represent the most constricted NPC state.

96
97 ***In cellulo* cryo-EM map of the *S. pombe* NPC**
98 To study NPC architecture and function *in cellulo* at the best possible resolution and structural
99 preservation, we explored various genetically tractable model organisms for their
100 compatibility with cryo-focused ion beam (FIB) specimen thinning, cryo-electron tomography
101 and subtomogram averaging (STA). *Saccharomyces cerevisiae* cells were compatible with high
102 throughput generation of cryo-lamellae and acquisition of tomograms. STA of their NPCs
103 resulted in moderately resolved structures (4). In contrast, a larger set of cryo-tomograms
104 from *Chaetomium thermophilum* cells did not yield any meaningful averages, possibly
105 because their NPCs displayed a very large structural variability. We therefore chose to work

Zimmerli, Allegretti et al

106 with *S. pombe* cells that are small enough for thorough vitrification, offer a superior geometry
107 for FIB-milling compared to *C. thermophilum* with the advantage of covering multiple cells
108 and, compared to *S. cerevisiae*, higher number of NEs and NPCs per individual cryo-lamellae
109 and tomogram, leading to high data throughput (**Fig. S1**).
110

111 To obtain a high quality cryo-EM map of *S. pombe* NPCs, we prepared cryo-FIB milled lamellae
112 of exponentially growing *S. pombe* cells and acquired 178 tomograms from which we
113 extracted 726 NPCs. Subsequent STA resulted in an *in cellulo* NPC average of very high quality
114 in terms of both visible features (**Fig. 1A, B and Fig. S2A**) and resolution (**Fig. S2B**). Systematic
115 fitting of the *S. pombe* IR asymmetric unit model (see Materials and Methods), resulted in a
116 highly significant fit (**Fig S3A**). The subsequent refinement with integrative modeling led to a
117 structural model that explains the vast majority of the observed electron optical density in
118 the IR (**Fig. 1B, Fig. S4, and Video S1**). The IR architecture appears reminiscent to NPC
119 structures of other eukaryotes (**Fig. S5**) further corroborating its evolutionary conservation
120 (1).

121
122 Although the outer rings are known to be more variable, the intra-subcomplex interaction
123 network of the Y-complex (Nup120, Nup85, Nup145C, Sec13, Nup84 and Nup133) has been
124 comprehensively characterized by many studies and considered to be conserved (1) (see
125 **Table S1** for nomenclature of Nups across different species). Systematic fitting revealed that
126 the NR of the SpNPC is composed of two concentric Y-complex rings (**Fig. 1A, Fig. S3B and**
127 **Video S1**) as in vertebrates and algae but as opposed to the single Y-complex ring observed
128 in *S. cerevisiae* (**Fig. S2A**) (4, 35, 38). Integrative modeling of the entire Y-complex ensemble
129 of the NR revealed a rather classical Y-complex architecture with the typical head-to-tail
130 oligomerization (**Fig. 2A and Fig. S4**). This analysis emphasizes that *S. pombe* Y-complex Nups
131 do localize to the NR, contrasting previous proposals (39). The homology models of SpNup131
132 and SpNup132 fit to the Y-complex tail region equally well, rendering these two proteins
133 indistinguishable by our approach.

134
135 Closer inspection of the cytoplasmic side of cryo-EM map revealed a surprising and
136 unprecedented architectural outline, since it did not form a ring. Instead, eight spatially
137 separated entities were observed (**Fig. 1A**) suggesting that the integrity of the cylindrical

Zimmerli, Allegretti et al

138 outline is rather provided by the IR and NR while the cytoplasmic protein entities serve as a
139 mere anchor point for the mRNA export platform, the Nup159 complex (**Fig. 2B**). Although
140 the dynein-arm that is characteristic for the *S. cerevisiae* NPC (40) is lacking, the Nup159
141 complex resembles its *S. cerevisiae* counterpart in shape (**Fig. S6A**). Systematic fitting and
142 subsequent refinement with integrative modeling revealed that the Y-complex vertex fits into
143 the density observed at the cytoplasmic side (**Fig. 2B, Fig. S3C, Fig. S4 and Video S1**). The
144 density potentially accounting for Nup107 and SpNup131/SpNup132 was missing (**Fig. S3D**)
145 and could not be recovered by local refinement (**Fig. S6B**). Instead, the observed density
146 sharply declined at the edge of SpNup189C consistent with previous work suggesting a split
147 of the SpNup189C-Nup107 interface (**Fig. S6C**) (39, 41). To independently confirm the identity
148 of the observed vertex-like density, we analyzed *nup37Δ* and *nup37Δ-ely5Δ* strains in which
149 non-essential, peripheral Y-complex Nups were deleted. The binding of both, Nup37 and Ely5
150 to Nup120 has been previously shown *in vitro* (42, 43), and as expected, density was missing
151 in the respective positions of all Y-complexes (**Fig. 2C-D and Fig. S7A-B**). Unexpectedly, a
152 density that could accommodate Ely5 homology model was missing also in the cytoplasmic Y-
153 complex, suggesting that Ely5 is present in *S. pombe* at both, the nuclear and the cytoplasmic
154 side of the NPC (**Fig 2D and Video S1**) unlike in higher metazoans where its homolog ELYS is
155 known to exclusively bind to the NR (35, 44). Otherwise, the NPC architecture remained
156 mostly unchanged, despite some increased flexibility in the Nup120 arm of the outer nuclear
157 Y-complex (**Fig. S7A-B**). These results unambiguously identify the density observed at the
158 cytoplasmic side as *bona fide* Y-complex vertex.

159

160 **Energy depletion leads to constriction of NPC scaffold and central channel**

161 Previous cryo-EM structures of NPCs obtained from isolated nuclear envelopes (32–37) or by
162 detergent extraction (45) had a smaller diameter as compared to those obtained from intact
163 cells (3, 4, 38, 46). We therefore hypothesized that NPC diameter may depend on the
164 biochemical energy level that is depleted during preparations of isolated nuclear envelopes
165 or NPCs but may also be reduced within intact cells e.g. during stress conditions. We set out
166 to systematically analyze the NPC architecture under conditions of energy depletion as
167 compared to exponentially growing cells. We structurally analyzed 292 NPCs subsequent to
168 1 hour of ED using non-hydrolysable 2-deoxy-glucose in combination with the respiratory
169 chain inhibitor antimycin A (see Materials and Methods). We measured the diameter based

Zimmerli, Allegretti et al

170 on centroids of the spokes as obtained by STA (see Materials and Methods) and found a
171 significant constriction of the mean central channel diameter during ED from ~70 nm to ~55
172 nm (**Fig. 3A**). The variation of diameters was larger within the population of NPCs exposed to
173 ED as compared to the actively transporting conditions, which likely blurred structural
174 features during STA. To generate a conformationally more homogenous ensemble, we split
175 the particles from the ED data set into two classes with central channel diameters of <50 nm
176 and >50 nm (533 and 1012 subunits respectively) (**Fig. 3B**) and refined them separately to <28
177 Å resolution (**Fig. 3C-D and Fig. S8A-B**). Both conformations of the ED state showed a smaller
178 NPC diameter compared to the control. The intermediate conformation was ~65 nm wide at
179 the IR while the most constricted conformation showed a diameter of ~49 nm (**Fig. 3D**) and
180 is thus comparable to the diameter observed in isolated NEs (32–37). We further calculated
181 the diameters at the level of the cytoplasmic side and NR and found that all three rings
182 constrict significantly during ED. While the diameter of the IR and cytoplasmic side changed
183 their conformation most dramatically, the NR was less affected (**Fig. 3E, Videos S4-S6**). The
184 estimated volume of the central channel in the most dilated state was almost twice as large
185 (~152'000 nm³) as compared to the most constricted state (~86'000 nm³) (**Fig. S8C**), which
186 likely translates to ~2-fold change in concentration of the FG-repeats contained therein.

187

188 To better understand how NPCs accommodate such massive conformational changes on the
189 molecular level, we systematically fitted individual subcomplexes (**Fig. S9**) and built structural
190 models of the three different diameter states based on the cryo-EM maps (**Fig. 3C-D**) using a
191 multi-state integrative modeling procedure (**Fig S4**). In the cytoplasmic side and the NR,
192 conformational changes were limited to the curvature of the Y-complexes and inward-
193 bending of the mRNA export platform towards the center of the pore (**Videos S4-6**). In
194 contrast, the central channel constriction of the IR is more elaborate and mediated by a lateral
195 displacement of the 8 spokes that move as independent entities to constrict or dilate the IR
196 (**Fig. 3D and Videos S4-S6**). In the dilated state, around 3-4 nm wide gaps are formed in-
197 between the neighboring spokes, while in the constricted state the spokes form extensive
198 contacts (**Fig. S10A-B**), equivalent to those in the previously published structures of the
199 human NPC in isolated nuclear envelopes (36). Notably, the spokes do not move entirely as
200 rigid bodies, but some conformational changes occur within the Nup155 and Nsp1 complex
201 regions (**Video S7 and S8**). Those are however distinct from the previously proposed

Zimmerli, Allegretti et al

202 conformational sliding (10) and rather consistent with an overall preserved intra-subcomplex
203 arrangement (15, 47).

204

205 Interestingly, under conditions of ED additional density is arching out into the lumen of the
206 NE (**Fig S10A and C**), contrasting control conditions under which they are less clearly
207 discernible from the membrane. It has been previously proposed that such luminal structures
208 are formed by Pom152 (ScPom152 or HsGP210) (48, 49). In terms of their shape, the observed
209 arches are reminiscent to those observed in isolated *Xenopus laevis* (34). Our data imply that
210 the luminal ring conformation becomes more prominent upon constriction. If this has any
211 mechanical benefits to keep NPCs separated (34), or might rather limit the maximal dilation,
212 remains to be further investigated.

213

214 **NPC constriction is concomitant with reduced diffusion and active nuclear transport**

215 We wondered about the transport competence of NPCs in conditions under which they are
216 constricted in comparison to actively transporting, dilated NPCs. To address this, we
217 employed live cell imaging of *S. pombe* cells expressing a GFP variant tagged with a nuclear
218 localization signal (NLS) on its N- and C-terminus (NLS-GFP) that shows a nuclear localization
219 under control conditions (**Fig. 4A**). Already after 30 min of ED most of the NLS-GFP localized
220 into the cytoplasm (**Fig. 4 B**), confirming that active nuclear import is suspended (26). To
221 assess passive diffusion across the nuclear envelope, we performed fluorescence recovery
222 after photobleaching (FRAP) experiments of nuclei in cells expressing freely diffusing GFP at
223 different time points after ED as compared to control conditions (**Fig. 4C and Fig. S11A-B**) (see
224 Materials and Methods). GFP diffusion rates into the nucleus were significantly decreased
225 upon energy depletion (**Fig. 4C**), contrasting a minor, negligible effect observed within the
226 cytoplasm (**Fig. S11C**). Passive diffusion was the slowest after about 1 hour of ED, the time at
227 which we structurally analyzed NPC architecture and is thus concomitant with NPC
228 constriction (**Fig. 4C**).

229

230 ED was shown to generally reduce cellular and nuclear volumes *S. pombe* cells (28, 29, 31).
231 We therefore hypothesized that changes of diameter of the NPC could be a result of a reduced
232 nuclear size that may reduce mechanical strain imposed onto the NPC scaffold by the nuclear
233 membranes. As a proxy for nuclear size we quantified the median nuclear projection surface

Zimmerli, Allegretti et al

234 and indeed found a highly significant reduction from $71 \mu\text{m}^2$ to $<60 \mu\text{m}^2$ under conditions of
235 ED (**Fig. 4D**), while NE staining based on Nup60-mCherry fluorescence indicated NE wrinkling
236 (**Fig. 4A**). This data therefore points to a general shrinkage of nuclei during ED. For a spherical
237 nucleus, the observed changes in nuclear projection area correspond to a reduction of $\sim 15\%$
238 in nuclear surface area and $\sim 25\%$ in nuclear volume, which would be sufficient to cause a loss
239 of NE tension (50) and may relax NPC scaffold into the constricted conformation (**Fig S12**).
240

241 **Discussion and Conclusion**

242 Here we have investigated the compositional and conformational plasticity of NPC
243 architecture in intact cells. We demonstrate that SpNPC scaffold exhibits an unexpected
244 subcomplex arrangement that is breaking the long-standing dogma of a three ringed
245 architecture. Similar to vertebrates and green algae, two concentric Y-complex rings form the
246 NR. On the cytoplasmic side, eight individual cytoplasmic Y-complex vertices that do not
247 exhibit any head-to-tail connection and thus do not form a ring. Although we cannot entirely
248 exclude that the Y-complex tail is flexible at the cytoplasmic side and was thus not resolved
249 during averaging, several lines of evidence argue against this. Previous biochemical analysis
250 was suggestive of less tightly associated tail and vertex portions of the Y-complex in *S. pombe*
251 (41). Another investigation suggested a non-isostoichiometric assembly of Y-complex
252 members *in vivo* (39) and structural analysis of the Y-complex from yet another fungus,
253 namely *Myceliophthora thermophila*, had demonstrated *in vitro* that Nup145C forms a stable
254 fold and associates with the vertex in absence of Nup107 (51). Although the Y-complex does
255 contain hinges (32, 51–54) that are likely important to facilitate large scale conformational
256 changes, the Nup189C-Nup107 interface is not known to be flexible. Taken together with the
257 fact that the observed electron optical density sharply declines at the respective site, it is very
258 likely that the interface between SpNup189C (HsNup96) and SpNup107, which was thought
259 to be conserved, is not formed in the cytoplasm but only in the nucleoplasm. A recent study
260 forced SpNup107 to the cytoplasmic side by expression of a SpNup189C-SpNup107 fusion
261 protein which led to re-localization of SpNup131 to the cytoplasmic side (39), and thus further
262 supports the here observed absence of the cytoplasmic Y-complex tail. How precisely *S.*
263 *pombe* cells spatially segregate the two different types of Y-complexes remains uncertain.
264 Our survey of public databases for splice variants, post-translational modifications and

Zimmerli, Allegretti et al

265 homologous structures did not yield significant clues. In contrast to vertebrates (35, 44), *S.*
266 *pombe* Ely5 is a member of both the nuclear and the cytoplasmic Y-complex vertex. It appears
267 plausible that ELYS acquired additional functional domains during evolution of open mitosis
268 in metazoans such as the C-terminal disordered region and AT-hook to tether Y-complexes to
269 NPC seeding sites on chromatin and consequently to the nuclear side of the NE.

270

271 We further show how conformational changes in NPC architecture mediate its constriction
272 and dilation within intact cells in response to a defined physiological cue, namely the energy
273 status of the cell. ED leads to a massive constriction of the central channel that results in a
274 ~2-fold loss in volume and is concomitant with a reduction of passive diffusion across the NE,
275 while active nuclear transport is completely shut down. If the observed reductions of
276 molecular exchange are directly or indirectly related to the NPC constriction remains
277 challenging to address, given the manifold processes occurring in cells entering quiescence in
278 response to ED (28–30, 55, 56). It however appears plausible that a reduction of the nuclear
279 pore central channel volume limits the diffusion rate. In fact it has been suggested that NPCs
280 reduce the diffusion rate of passively translocating molecules in response to their molecular
281 size, rather than showing a strict size exclusion threshold (57). It has been further shown that
282 active nuclear transport does not enhance passive diffusion (58, 59) and several studies have
283 shown that cytoplasmic diffusion of small proteins, such as soluble mCherry, is not
284 significantly affected during ED (28). Finally, a recent study showed that the uptake and
285 partitioning of both passively diffusing and nuclear transport factor (NTF)-like molecules by
286 FG-domain *in vitro* is directly dependent on the their concentration (60). All of which agrees
287 well with our findings. It therefore is plausible that a constricted central channel volume leads
288 to an increased local FG-domain concentration which in turn limits the passive diffusion of
289 molecules of a constant size, similar to the diffusion limitation observed in response to
290 increasing molecular size under control conditions.

291

292 Peripheral channels are thought to be important for the nuclear import of inner nuclear
293 membrane proteins (11–13). Here we observed around 3–4 nm wide lateral gaps between the
294 individual spokes of actively transporting NPCs. Notably, our data processing workflow yields
295 an average of conformation under the respective conditions and individual spokes are even

Zimmerli, Allegretti et al

296 more dynamic ((6) and this study). Therefore, it is plausible that the opening and closing of
297 peripheral channels may regulate the translocation of inner nuclear membrane proteins.

298

299 Based on crystal structures of fragments of the Nsp1 (HsNup62) complex, it had been
300 previously suggested that NPCs undergo dilation cycles that involve refolding and alternative
301 configurations of the coiled-coil domains of the complex (61). The conformational changes
302 observed in this study are very different. They do not necessitate a rearrangement of
303 subcomplex folds but are rather based on large scale movements (**Videos S4-S7**). Such
304 movements may also be relevant during NPC assembly or turnover, where significant smaller
305 diameters have been observed (4, 8, 9).

306

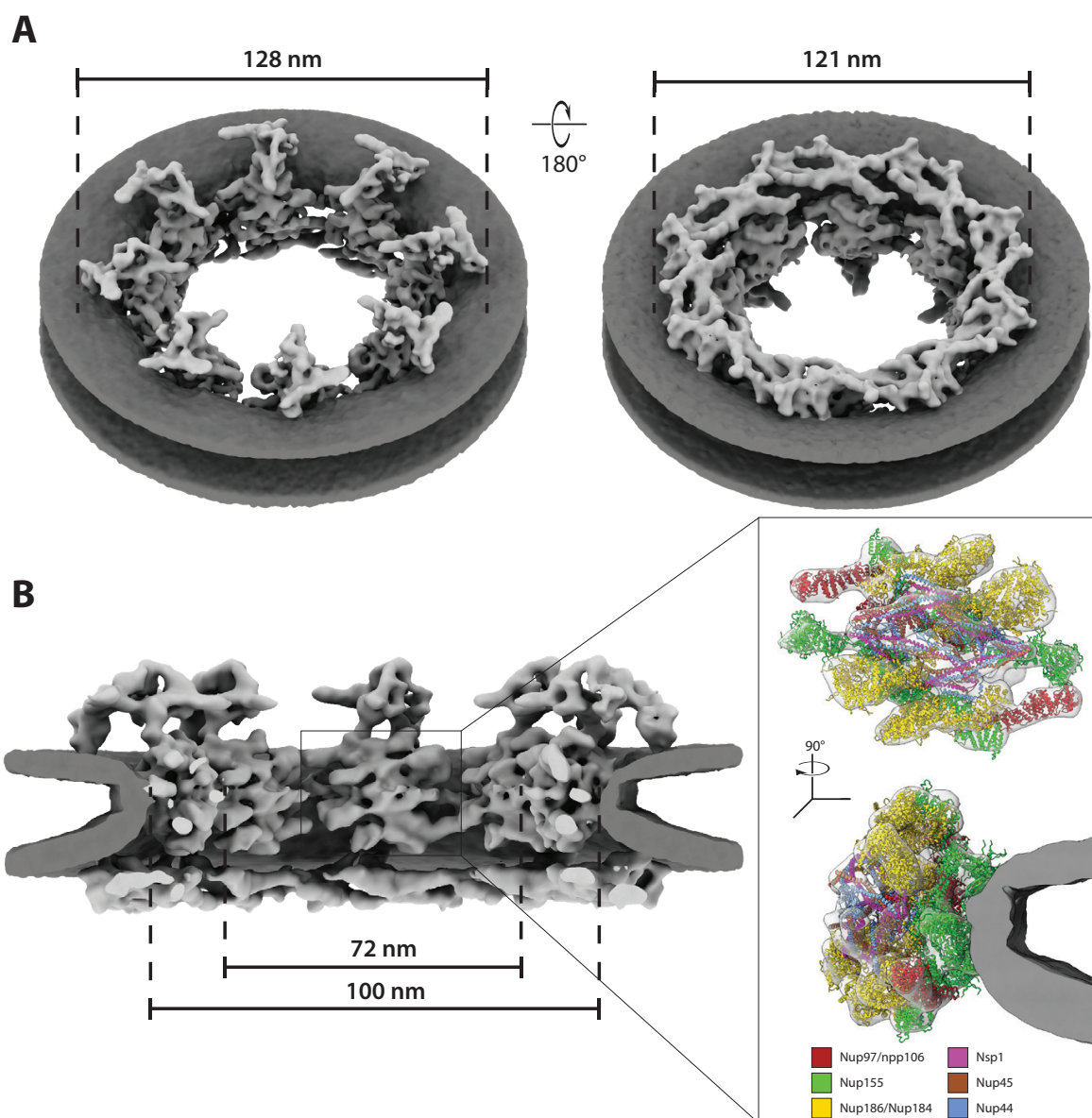
307 How ED mechanically leads to NPC constriction remains to be further addressed in the future.
308 It appears likely that a reduced nuclear volume relieves NE tension and in turn allows NPCs to
309 constrict (50). At this point, we cannot exclude additional factors such as the previously
310 reported cellular pH-change during ED (28, 29) or the shut-down of active nuclear transport
311 itself to have an effect on NTF occupancy and NPC conformation. However, mechanical
312 tension on the NE and active nuclear transport are certainly diminished during NE or NPC
313 isolation. Therefore, previous structural analysis of such preparations has yielded structures
314 that correspond to the most constricted conformation at the very end of the scale.

315

316 In conclusion we show that NPCs within living cells populate a much larger conformational
317 space and thereby confirm their importance as regulators of nucleocytoplasmic transport in
318 response to environmental cues in living organisms on a cellular level. Hence our study
319 highlights the power and importance of *in cellulo* structural analyzes to study such crucial
320 physiological processes at the macromolecular level within the relevant cellular environment.

Zimmerli, Allegretti et al

321



322

323 **Figure 1. *In cellulo* cryo-EM map of the *S. pombe* NPC.** A) Isosurface rendered views of the *S.*

324 *pombe* NPC as seen from the cytoplasm (left) and the nucleoplasm (right; with membranes in

325 dark and protein in light grey). While the cytoplasmic view (left) reveals eight disconnected

326 protein entities instead of a cytoplasmic ring, the nuclear view (right) shows two concentric

327 nuclear Y-complex rings. B) Same as (A) but shown as cutaway view. While the asymmetric

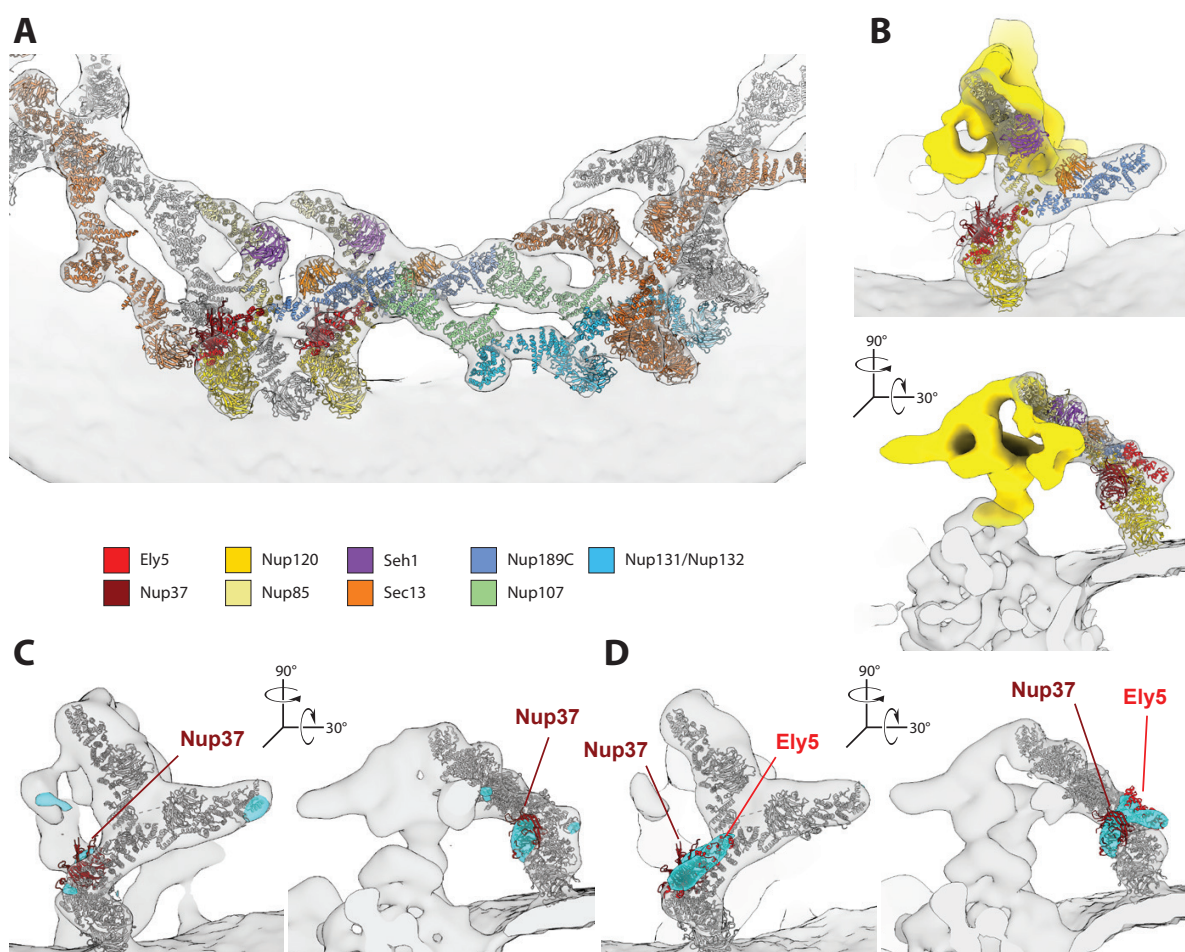
328 curvature of the nuclear membranes and the arrangement of the cytoplasmic side is

329 unprecedented in other species, the inner ring architecture is highly conserved as highlighted

330 in the inset (see also **Fig. S5**). Fitting of inner ring nucleoporin homology models explains the

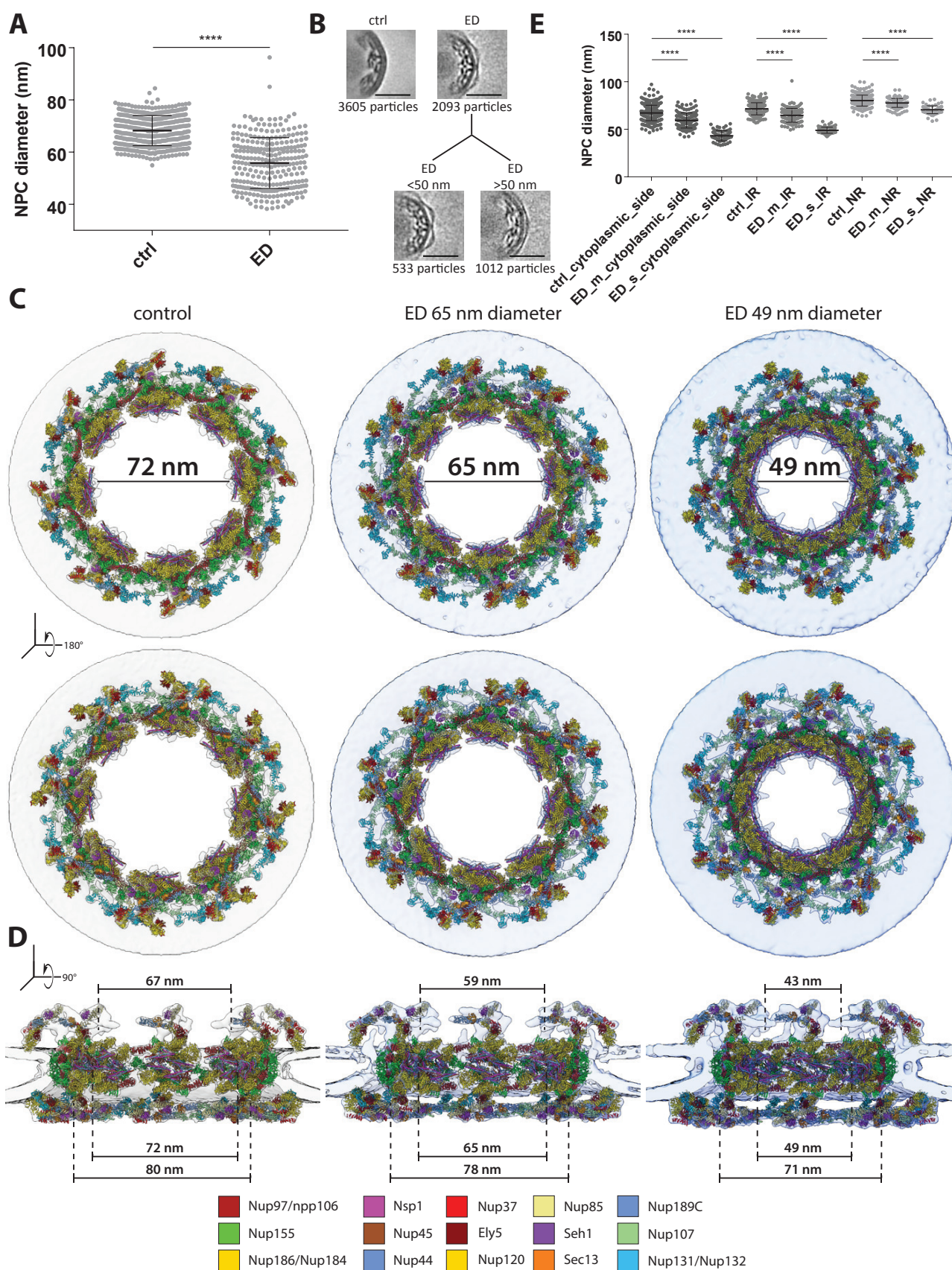
331 vast majority of the observed electron optical density.

332



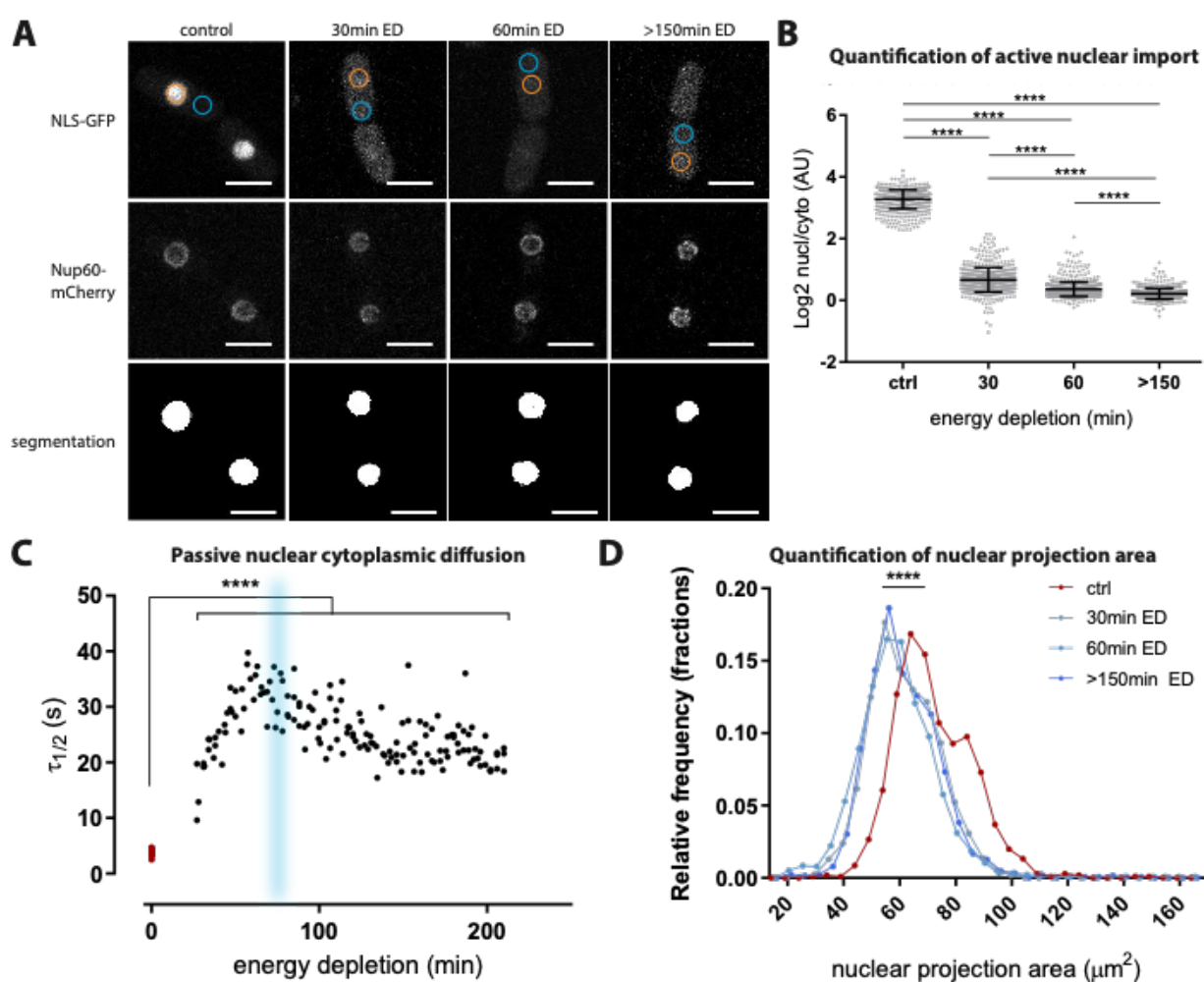
333

334 **Figure 2. Architecture of spNPC outer rings.** A) Systematic fitting and integrative modeling of
335 all *S. pombe* Y-complex nucleoporins reveals a head-to-tail arrangement with two concentric
336 Y-complex rings on the nuclear side of the SpNPC similar to humans. A segment of the NR of
337 the cryo-EM map is shown isosurface rendered in transparent light grey. The adjacent inner
338 Y-complexes are shown in grey and outer Y-complexes are shown in orange. B) Integrative
339 model of the cytoplasmic protein entities. The fit of the Y-complex vertex explains most of
340 the observed density. The mRNA export platform as identified in (4, 62) is segmented in
341 yellow. C, D) Verification of the molecular identity of the observed structure. C) The *nup37Δ*
342 cryo-EM map is shown in light grey and overlaid with the difference map (cyan) of the *wild*
343 type and *nup37Δ* maps, both filtered to 27 Å. The missing density in the long arm of the Y-
344 vertex coincidences with the position of Nup37 (dark red) of the Y-complex vertex (dark grey,
345 as in A). D) *nup37Δ-ely5Δ* double knockout map (light grey) overlaid with the corresponding
346 difference map (cyan). Differences are apparent at the location of both, Nup37 (dark red) and
347 Ely5 (light red) with respect to the fitted Y-complex model (dark grey).



Zimmerli, Allegretti et al

349 **Figure 3. NPCs constrict upon energy depletion.** A) Diameter measurement of control
350 (n=438) and energy depleted (n=271) NPCs based on subunit positions obtained by STA (see
351 Materials and methods) reveals a significant constriction of NPCs upon ED (mean \pm standard
352 error of mean (SdEM) control: 68.2 nm and mean ED: 55.84 nm, whiskers indicate standard
353 deviation, p-value < 0.0001, two-sided t-test). B) Slices through subtomogram averages
354 corresponding to (A) show the different conformations at the level of the IR. NPCs were
355 divided into two classes with diameters of <50 nm (left) and >50 nm (right; scale bar: 50
356 nm). C) Measurements of individual NPC diameters at the CR, IR and NR in control
357 conditions and during ED reveal significant diameter constriction of all three rings (all p-
358 values <0.0001; ctrl control; ED_m represents the class with diameter of >50nm; ED_s
359 represents the class with diameter of <50 nm. Diameters mean \pm SdEM measured are: 67.25
360 \pm 0.44, n=341 (ctrl_cytoplasmic_side); 59.29 \pm 0.6817, n=136 (ED_m_cytoplasmic_side) and
361 43.15 \pm 0.6509, n=68 (ED_s_cytoplasmic_side); 71.59 \pm 0.3459, n=341 (ctrl_IR); 64.73 \pm
362 0.626, n=136 (ED_m_IR) and 49 \pm 0.3815, n=68 (ED_s_IR); 80.22 \pm 0.3106, n=341 (ctrl_NR);
363 77.71 \pm 0.4006, n=136 (ED_m_NR) and 70.59 \pm 0.5001, n=68, whiskers indicate standard
364 deviation. D) Cytoplasmic view (top) and nuclear view (bottom) of cryo-EM maps
365 superimposed with the respective integrative models from actively transporting,
366 intermediate and fully constricted NPCs illustrating the overall conformational change
367 leading to a central channel diameter constriction from 72 nm to 49 nm. The cytoplasmic
368 and IR spokes move as individual entities and contribute the most to the central channel
369 diameter change, whereas the NR constricts to a lesser extent. E) Same as (D) but show as
370 cutaway side view. Upon constriction, the mRNA export platform bends towards the center
371 of the NPC. Conformational changes of the NR are less dramatic and include mostly changes
372 in the curvature of the Y complexes (see also supplementary videos 4-8).
373



374 **Figure 4 How energy depletion affects transport across the nuclear envelope and nuclear**
375 **size. A)** Maximum projected confocal stack from life cell imaging of NLS-GFP and Nup60-
376 mCherry are used to measure active nuclear transport and nuclear size during energy
377 depletion. Actively imported NLS-GFP loses its nuclear localization during ED indicating a
378 shutdown of active nuclear transport during ED. The nuclear projection area is reduced during
379 ED as determined by segmenting the Nup60-mCherry NE signal, indicating a reduced nuclear
380 volume. Orange (nuclear) and blue (cytoplasmic) circles indicate areas used for quantification
381 of the GFP signal. Nuclear projection areas were determined in the mCherry-channel using
382 automated segmentation (see Materials and Methods) (scale bar: 5μm). **B)** Quantification of
383 nuclear/cytoplasmic signal shows a significant leakage of NLS-GFP into the cytoplasm and thus
384 indicates a shutdown of active nuclear transport already after 30 min of ED. The observed
385 mean log2 fold change were: 3.276 (n=623) under control conditions; 0.662 (n=584) after 30
386 min; 0.3654 (n=722) 60 min and 0.2144 (n=604) >150 min after ED (all adjusted p-values
387 <0.0001, ordinary one-way ANOVA and Tukey's multiple comparison test). **C)** FRAP-recovery

Zimmerli, Allegretti et al

389 half-life times of nuclear signal from freely diffusing GFP at various time points after ED are
390 significantly longer during ED as compared to control conditions (red dots) (p-value <0.0001,
391 two-sided unpaired t-test) indicating a general down regulation of passive diffusion under
392 these conditions. Passive nuclear diffusion of free GFP reaches a minimum after \sim 1 hour of
393 ED and subsequently recovers slightly, pointing to cellular adaptation. The blue area shows
394 the timepoint at which cryo-EM grids were prepared for structural analysis of ED NPCs. D)
395 Histogram of quantified nuclear projection areas measured in segmented mCherry-channel
396 of life-cell imaging as shown in (A) reveal a significant shift towards smaller values during ED
397 (blue curves) as compared to control conditions (red curve) indicating a general loss of nuclear
398 volume during ED that also manifest in NE wrinkling as seen in (A) (all adjusted p-values are
399 <0.0001, one-way ordinary ANOVA and Holm-Sidak's multiple comparison test with n=1056
400 control, n=1168 30min, n=2153 60min and n=1255 >150min after ED).

401

402

403

404 **Supplementary Material**

405

406 **Materials and Methods**

407 **Supplementary figures 1-12**

408 **Supplementary tables 1-3**

409 **Supplementary videos 1-7**

410

411 **Author contributions**

412 CEZ conceived the project, designed and performed experiments, acquired all types of data,
413 designed and established data analysis procedures, analyzed all types of data, wrote the
414 manuscript; MA conceived the project, designed and performed experiments, acquired data,
415 analyzed data, wrote the manuscript; VR analyzed data, wrote the manuscript; SG designed
416 and performed experiments, acquired data; AOK analyzed data; IZ designed and performed
417 experiments; AH designed and performed experiments; JM designed experiments, supervised
418 the project, JK conceived the project, designed and established data analysis procedures,

Zimmerli, Allegretti et al

419 analyzed data, supervised the project, wrote the manuscript; MB conceived the project,
420 designed experiments, supervised the project, wrote the manuscript.

421

422 Competing interests

423 Authors declare no competing interests.

424

425 Data availability

426 Associated with the manuscript are accession numbers EMD-11373, EMD-11374, EMD-
427 11375. Integrative models will be deposited into the PDBDEV upon publication. The code,
428 along the input files, for the modeling will be deposited in Zenodo upon publication.

429

430 Acknowledgements

431 We thank Beata Turoňová, Nikola Kellner, Wim Hagen, Felix Weiss, Christian Tischer, Janina
432 Baumbach, Ed Hurt, Edward Lemke as well as all the members of the Mahamid, Kosinski and
433 Beck laboratories for advice and support. We thank Ed Hurt, Buzz Baum, Thomas Schwartz
434 and Christian Häring for providing yeast strains. We acknowledge support from the Electron
435 Microscopy Core Facility, the Advanced Light Microscopy Facility and IT services of EMBL
436 Heidelberg. MA was funded by an EMBO a long-term fellowship (ALTF-1389-2016); JM
437 received funding from the European Research Council (ERC 3DCellPhase 760067). MB
438 acknowledges funding by EMBL, the Max Planck Society and the European Research Council
439 (ComplexAssembly 724349).

440

441

442 References

- 443 1. D. H. Lin, A. Hoelz, The Structure of the Nuclear Pore Complex (An Update). *Annu.
444 Rev. Biochem.* **88**, 725–783 (2019).
- 445 2. M. Beck, S. Mosalaganti, J. Kosinski, From the resolution revolution to evolution:
446 structural insights into the evolutionary relationships between vesicle coats and the
447 nuclear pore. *Curr. Opin. Struct. Biol.* **52**, 32–40 (2018).
- 448 3. J. Mahamid, S. Pfeffer, M. Schaffer, E. Villa, R. Danev, L. K. Cuellar, F. Förster, A. A.

449 Hyman, J. M. Plitzko, W. Baumeister, Visualizing the molecular sociology at the HeLa
450 cell nuclear periphery. *Science (80-.)*. **351**, 969–972 (2016).

451 4. M. Allegretti, C. E. Zimmerli, V. Rantos, F. Wilfling, P. Ronchi, H. K. H. Fung, C.-W. Lee,
452 W. Hagen, B. Turonova, K. Karius, X. Zhang, C. Müller, Y. Schwab, J. Mahamid, B.
453 Pfander, J. Kosinski, M. Beck, In cell architecture of the nuclear pore complex and
454 snapshots of its turnover. *in revision* (2020).

455 5. G. J. Stanley, A. Fassati, B. W. Hoogenboom, Atomic force microscopy reveals
456 structural variability amongst nuclear pore complexes. *Life Sci. Alliance*. **1** (2018),
457 doi:10.26508/lsa.201800142.

458 6. M. Beck, V. Lüí, F. Förster, W. Baumeister, O. Medalia, V. Lucić, F. Förster, W.
459 Baumeister, O. Medalia, Snapshots of nuclear pore complexes in action captured by
460 cryo-electron tomography. *Nature*. **449**, 611–615 (2007).

461 7. J. Sellés, M. Penrad-Mobayed, C. Guillaume, A. Fuger, L. Auvray, O. Faklaris, F.
462 Montel, Nuclear pore complex plasticity during developmental process as revealed by
463 super-resolution microscopy. *Sci. Rep.* **7** (2017), doi:10.1038/s41598-017-15433-2.

464 8. S. Otsuka, A. M. Steyer, M. Schorb, J. K. Hériché, M. J. Hossain, S. Sethi, M. Kueblbeck,
465 Y. Schwab, M. Beck, J. Ellenberg, Postmitotic nuclear pore assembly proceeds by
466 radial dilation of small membrane openings. *Nat. Struct. Mol. Biol.* **25**, 21–28 (2018).

467 9. S. Otsuka, K. H. Bui, M. Schorb, M. Julius Hossain, A. Z. Politi, B. Koch, M. Eltsov, M.
468 Beck, J. Ellenberg, Nuclear pore assembly proceeds by an inside-out extrusion of the
469 nuclear envelope. *eLife*. **5** (2016), doi:10.7554/eLife.19071.

470 10. J. Koh, G. Blobel, Allosteric regulation in gating the central channel of the nuclear
471 pore complex. *Cell*. **161**, 1361–1373 (2015).

472 11. A. C. Meinema, J. K. Laba, R. A. Hapsari, R. Otten, F. A. A. Mulder, A. Kral, G. Van Den
473 Bogaart, C. P. Lusk, B. Poolman, L. M. Veenhoff, Long unfolded linkers facilitate
474 membrane protein import through the nuclear pore complex. *Science (80-.)*. **333**, 90–
475 93 (2011).

476 12. R. Ungrich, M. Klann, P. Horvath, U. Kutay, Diffusion and retention are major
477 determinants of protein targeting to the inner nuclear membrane. *J. Cell Biol.* **209**,
478 687–704 (2015).

479 13. A. Boni, A. Z. Politi, P. Strnad, W. Xiang, M. J. Hossain, J. Ellenberg, Live imaging and
480 modeling of inner nuclear membrane targeting reveals its molecular requirements in

481 mammalian cells. *J. Cell Biol.* **209**, 705–720 (2015).

482 14. H. Chug, S. Trakhanov, B. B. Hülsmann, T. Pleiner, D. Görlich, Crystal structure of the
483 metazoan Nup62•Nup58•Nup54 nucleoporin complex. *Science (80-.)* **350**, 106–110
484 (2015).

485 15. T. Stuwe, C. J. Bley, K. Thierbach, S. Petrovic, S. Schilbach, D. J. Mayo, T. Perriches, E. J.
486 Rundlet, Y. E. Jeon, L. N. Collins, F. M. Huber, D. H. Lin, M. Paduch, A. Koide, V. Lu, J.
487 Fischer, E. Hurt, S. Koide, A. A. Kossiakoff, A. Hoelz, Architecture of the fungal nuclear
488 pore inner ring complex. *Science (80-.)* **350**, 56–64 (2015).

489 16. V. Shahin, T. Danker, K. Enss, R. Ossig, H. Oberleithner, Evidence for Ca²⁺- and ATP-
490 sensitive peripheral channels in nuclear pore complexes. *FASEB J.* **15**, 1895–1901
491 (2001).

492 17. D. Stoffler, K. N. Goldie, B. Feja, U. Aebi, Calcium-mediated structural changes of
493 native nuclear pore complexes monitored by time-lapse atomic force microscopy. *J.
494 Mol. Biol.* **287**, 741–752 (1999).

495 18. A. Rakowska, T. Danker, S. W. Schneider, H. Oberleithner, ATP-induced shape change
496 of nuclear pores visualized with the atomic force microscope. *J. Membr. Biol.* **163**,
497 129–136 (1998).

498 19. L. Kastrup, H. Oberleithner, Y. Ludwig, C. Schafer, V. Shahin, Nuclear envelope barrier
499 leak induced by dexamethasone. *J. Cell. Physiol.* **206**, 428–434 (2006).

500 20. I. Liashkovich, A. Meyring, A. Kramer, V. Shahin, Exceptional structural and
501 mechanical flexibility of the nuclear pore complex. *J. Cell. Physiol.* **226**, 675–682
502 (2011).

503 21. R. D. Jäggi, A. Franco-Obregón, P. Mühlhäuser, F. Thomas, U. Kutay, K. Ensslin,
504 Modulation of nuclear pore topology by transport modifiers. *Biophys. J.* **84**, 665–670
505 (2003).

506 22. D. Görlich, N. Panté, U. Kutay, U. Aebi, F. R. Bischoff, Identification of different roles
507 for RanGDP and RanGTP in nuclear protein import. *EMBO J.* **15**, 5584–5594 (1996).

508 23. M. Stewart, Nuclear export of mRNA. *Trends Biochem. Sci.* **35** (2010), pp. 609–617.

509 24. W. D. Richardson, A. D. Mills, S. M. Dilworth, R. A. Laskey, C. Dingwall, Nuclear protein
510 migration involves two steps: Rapid binding at the nuclear envelope followed by
511 slower translocation through nuclear pores. *Cell.* **52**, 655–664 (1988).

512 25. N. Shulga, P. Roberts, Z. Gu, L. Spitz, M. M. Tabb, M. Nomura, D. S. Goldfarb, “In vivo

513 nuclear transport kinetics in *Saccharomyces cerevisiae*: A role for heat shock protein
514 70 during targeting and translocation" (1996), , doi:10.1083/jcb.135.2.329.

515 26. W. A. Whalen, J. H. Yoon, R. Shen, R. Dhar, Regulation of mRNA export by nutritional
516 status in fission yeast. *Genetics*. **152**, 827–838 (1999).

517 27. E. D. Schwoebel, T. H. Ho, M. S. Moore, The mechanism of inhibition of Ran-
518 dependent nuclear transport by cellular ATP depletion. *J. Cell Biol.* **157**, 963–974
519 (2002).

520 28. M. C. Munder, D. Midtvedt, T. Franzmann, E. Nüske, O. Otto, M. Herbig, E. Ulbricht, P.
521 Müller, A. Taubenberger, S. Maharana, L. Malinovska, D. Richter, J. Guck, V.
522 Zaburdaev, S. Alberti, A pH-driven transition of the cytoplasm from a fluid- to a solid-
523 like state promotes entry into dormancy. *eLife*. **5** (2016), doi:10.7554/eLife.09347.

524 29. R. P. Joyner, J. H. Tang, J. Helenius, E. Dultz, C. Brune, L. J. Holt, S. Huet, D. J. Müller, K.
525 Weis, A glucose-starvation response regulates the diffusion of macromolecules. *eLife*.
526 **5** (2016), doi:10.7554/eLife.09376.

527 30. G. Marini, E. Nüske, W. Leng, S. Alberti, G. Pigino, Reorganization of budding yeast
528 cytoplasm upon energy depletion. *Mol. Biol. Cell*. **31**, 1232–1245 (2020).

529 31. M. B. Heimlicher, M. Bächler, M. Liu, C. Ibeneche-Nnewihe, E. L. Florin, A. Hoenger, D.
530 Brunner, Reversible solidification of fission yeast cytoplasm after prolonged nutrient
531 starvation. *J. Cell Sci.* **132** (2019), doi:10.1242/jcs.231688.

532 32. K. H. Bui, A. Von Appen, A. L. Diguilio, A. Ori, L. Sparks, M. T. Mackmull, T. Bock, W.
533 Hagen, A. Andrés-Pons, J. S. Glavy, M. Beck, Integrated structural analysis of the
534 human nuclear pore complex scaffold. *Cell*. **155**, 1233–1243 (2013).

535 33. M. Eibauer, M. Pellanda, Y. Turgay, A. Dubrovsky, A. Wild, O. Medalia, Structure and
536 gating of the nuclear pore complex. *Nat. Commun.* **6** (2015),
537 doi:10.1038/ncomms8532.

538 34. Y. Zhang, S. Li, C. Zeng, G. Huang, X. Zhu, Q. Wang, K. Wang, Q. Zhou, C. Yan, W.
539 Zhang, G. Yang, M. Liu, Q. Tao, J. Lei, Y. Shi, Molecular architecture of the luminal ring
540 of the *Xenopus laevis* nuclear pore complex. *Cell Res.* **30**, 532–540 (2020).

541 35. A. von Appen, J. Kosinski, L. Sparks, A. Ori, A. L. DiGuilio, B. Vollmer, M.-T. T.
542 Mackmull, N. Banterle, L. Parca, P. Kastritis, K. Buczak, S. Mosalaganti, W. Hagen, A.
543 Andres-Pons, E. A. Lemke, P. Bork, W. Antonin, J. S. Glavy, K. H. Bui, M. Beck, In situ
544 structural analysis of the human nuclear pore complex. *Nature*. **526**, 140–143 (2015).

545 36. J. Kosinski, S. Mosalaganti, A. Von Appen, R. Teimer, A. L. Diguilio, W. Wan, K. H. Bui,
546 W. J. H. Hagen, J. A. G. Briggs, J. S. Glavy, E. Hurt, M. Beck, Molecular architecture of
547 the inner ring scaffold of the human nuclear pore complex. *Science (80-.)* **352**, 363–
548 365 (2016).

549 37. G. Huang, Y. Zhang, X. Zhu, C. Zeng, Q. Wang, Q. Zhou, Q. Tao, M. Liu, J. Lei, C. Yan, Y.
550 Shi, Structure of the cytoplasmic ring of the *Xenopus laevis* nuclear pore complex by
551 cryo-electron microscopy single particle analysis. *Cell Res.* **30**, 520–531 (2020).

552 38. S. Mosalaganti, J. Kosinski, S. Albert, M. Schaffer, D. Strenkert, P. A. Salomé, S. S.
553 Merchant, J. M. Plitzko, W. Baumeister, B. D. Engel, M. Beck, In situ architecture of
554 the algal nuclear pore complex. *Nat. Commun.* **9**, 2361 (2018).

555 39. H. Asakawa, T. Kojidani, H. J. Yang, C. Ohtsuki, H. Osakada, A. Matsuda, M. Iwamoto,
556 Y. Chikashige, K. Nagao, C. Obuse, Y. Hiraoka, T. Haraguchi, Asymmetrical localization
557 of nup107-160 subcomplex components within the nuclear pore complex in fission
558 yeast. *PLoS Genet.* **15**, 223131 (2019).

559 40. P. Stelter, R. Kunze, D. Flemming, D. Höpfner, M. Diepholz, P. Philippsen, B. Böttcher,
560 E. Hurt, Molecular basis for the functional interaction of dynein light chain with the
561 nuclear-pore complex. *Nat. Cell Biol.* **9**, 788–796 (2007).

562 41. S. W. Bai, J. Rouquette, M. Umeda, W. Faigle, D. Loew, S. Sazer, V. Doye, The Fission
563 Yeast Nup107-120 Complex Functionally Interacts with the Small GTPase Ran/Spi1
564 and Is Required for mRNA Export, Nuclear Pore Distribution, and Proper Cell Division.
565 *Mol. Cell. Biol.* **24**, 6379–6392 (2004).

566 42. X. Liu, J. M. Mitchell, R. W. Wozniak, G. Blobel, J. Fan, Structural evolution of the
567 membrane-coating module of the nuclear pore complex. *Proc. Natl. Acad. Sci. U. S. A.*
568 **109**, 16498–16503 (2012).

569 43. S. Bilokapic, T. U. Schwartz, Molecular basis for Nup37 and ELY5/ELYS recruitment to
570 the nuclear pore complex. *Proc. Natl. Acad. Sci. U. S. A.* **109**, 15241–15246 (2012).

571 44. B. A. Rasala, A. V. Orjalo, Z. Shen, S. Briggs, D. J. Forbes, ELYS is a dual
572 nucleoporin/kinetochore protein required for nuclear pore assembly and proper cell
573 division. *Proc. Natl. Acad. Sci. U. S. A.* **103**, 17801–17806 (2006).

574 45. S. J. Kim, J. Fernandez-Martinez, I. Nudelman, Y. Shi, W. Zhang, B. Raveh, T. Herricks,
575 B. D. Slaughter, J. A. Hogan, P. Upla, I. E. Chemmama, R. Pellarin, I. Echeverria, M.
576 Shivaraju, A. S. Chaudhury, J. Wang, R. Williams, J. R. Unruh, C. H. Greenberg, E. Y.

577 Jacobs, Z. Yu, M. J. De La Cruz, R. Mironksa, D. L. Stokes, J. D. Aitchison, M. F. Jarrold,
578 J. L. Gerton, S. J. Ludtke, C. W. Akey, B. T. Chait, A. Sali, M. P. Rout, Integrative
579 structure and functional anatomy of a nuclear pore complex. *Nature*. **555**, 475–482
580 (2018).

581 46. T. Maimon, N. Elad, I. Dahan, O. Medalia, The human nuclear pore complex as
582 revealed by cryo-electron tomography. *Structure*. **20**, 998–1006 (2012).

583 47. H. Chug, S. Trakhanov, B. B. Hülsmann, T. Pleiner, D. Görlich, Crystal structure of the
584 metazoan Nup62•Nup58•Nup54 nucleoporin complex. *Science (80-.).* **350**, 106–110
585 (2015).

586 48. R. W. Wozniak, G. Blobel, M. P. Rout, POM152 is an integral protein of the pore
587 membrane domain of the yeast nuclear envelope. *J. Cell Biol.* **125**, 31–42 (1994).

588 49. P. Upla, S. J. Kim, P. Sampathkumar, K. Dutta, S. M. Cahill, I. E. Chemmama, R.
589 Williams, J. B. Bonanno, W. J. Rice, D. L. Stokes, D. Cowburn, S. C. Almo, A. Sali, M. P.
590 Rout, J. Fernandez-Martinez, Molecular Architecture of the Major Membrane Ring
591 Component of the Nuclear Pore Complex. *Structure*. **25**, 434–445 (2017).

592 50. A. Elosegui-Artola, I. Andreu, A. E. M. Beedle, A. Lezamiz, M. Uroz, A. J. Kosmalska, R.
593 Oria, J. Z. Kechagia, P. Rico-Lastres, A. L. Le Roux, C. M. Shanahan, X. Trepat, D.
594 Navajas, S. Garcia-Manyes, P. Roca-Cusachs, Force Triggers YAP Nuclear Entry by
595 Regulating Transport across Nuclear Pores. *Cell*. **171**, 1397-1410.e14 (2017).

596 51. K. Kelley, K. E. Knockenhauer, G. Kabachinski, T. U. Schwartz, Atomic structure of the
597 γ complex of the nuclear pore. *Nat. Struct. Mol. Biol.* **22**, 425–431 (2015).

598 52. K. Thierbach, A. von Appen, M. Thoms, M. Beck, D. Flemming, E. Hurt, Protein
599 Interfaces of the Conserved Nup84 Complex from *Chaetomium thermophilum* Shown
600 by Crosslinking Mass Spectrometry and Electron Microscopy. *Structure*. **21**, 1672–
601 1682 (2013).

602 53. S. Krull, J. Dörries, B. Boysen, S. Reidenbach, L. Magnus, H. Norder, J. Thyberg, V. C.
603 Cordes, Protein Tpr is required for establishing nuclear pore-associated zones of
604 heterochromatin exclusion. *EMBO J.* **29**, 1659–1673 (2010).

605 54. S. A. Nordeen, D. L. Turman, T. U. Schwartz, *bioRxiv*, in press,
606 doi:10.1101/2020.06.19.161133.

607 55. E. Nüske, G. Marini, D. Richter, W. Leng, A. Bogdanova, T. M. Franzmann, G. Pigino, S.
608 Alberti, *Biol. Open*, in press, doi:10.1242/bio.046391.

609 56. B. R. Parry, I. V. Surovtsev, M. T. Cabeen, C. S. O'Hern, E. R. Dufresne, C. Jacobs-
610 Wagner, The bacterial cytoplasm has glass-like properties and is fluidized by
611 metabolic activity. *Cell.* **156**, 183–194 (2014).

612 57. B. L. Timney, B. Raveh, R. Mironksa, J. M. Trivedi, S. J. Kim, D. Russel, S. R. Wente, A.
613 Sali, M. P. Rout, Simple rules for passive diffusion through the nuclear pore complex.
614 *J. Cell Biol.* **215** (2016), doi:10.1083/jcb.201601004.

615 58. S. Frey, D. Görlich, FG/FxFG as well as GLFG repeats form a selective permeability
616 barrier with self-healing properties. *EMBO J.* **28**, 2554–2567 (2009).

617 59. D. Mohr, S. Frey, T. Fischer, T. Gütter, D. Görlich, Characterisation of the passive
618 permeability barrier of nuclear pore complexes. *EMBO J.* **28**, 2541–2553 (2009).

619 60. R. Frost, D. Débarre, S. Jana, F. Bano, J. Schünemann, D. Görlich, R. P. Richter, “A
620 method to quantify molecular diffusion within thin solvated polymer films: A case
621 study on films of natively unfolded nucleoporins.”

622 61. S. R. Solmaz, G. Blobel, I. Melcák, Ring cycle for dilating and constricting the nuclear
623 pore. *Proc. Natl. Acad. Sci. U. S. A.* **110**, 5858–5863 (2013).

624 62. J. Fernandez-Martinez, S. J. Kim, Y. Shi, P. Upla, R. Pellarin, M. Gagnon, I. E.
625 Chemmama, J. Wang, I. Nudelman, W. Zhang, R. Williams, W. J. Rice, D. L. Stokes, D.
626 Zenklusen, B. T. Chait, A. Sali, M. P. Rout, Structure and Function of the Nuclear Pore
627 Complex Cytoplasmic mRNA Export Platform. *Cell.* **167**, 1215-1228.e25 (2016).

628 63. N. Kellner, J. Schwarz, M. Sturm, J. Fernandez-Martinez, S. Griesel, W. Zhang, B. T.
629 Chait, M. P. Rout, U. Kück, E. Hurt, Developing genetic tools to exploit *Chaetomium*
630 *thermophilum* for biochemical analyses of eukaryotic macromolecular assemblies.
631 *Sci. Rep.* **6**, 20937 (2016).

632 64. H. Amelina, V. Moiseeva, L. C. Collopy, S. R. Pearson, C. A. Armstrong, K. Tomita,
633 Sequential and counter-selectable cassettes for fission yeast. *BMC Biotechnol.* **16**, 76
634 (2016).

635 65. J. Bähler, J. Wu, M. S. Longtine, N. G. Shah, A. M. III, A. B. Steever, A. Wach, P.
636 Philippse, J. R. Pringle, Heterologous modules for efficient and versatile PCR-based
637 gene targeting in *Schizosaccharomyces pombe*. *Yeast.* **14**, 943–951 (1998).

638 66. G. Dey, S. Culley, S. A. Curran, R. Henriques, W. Kukulski, B. Baum, Closed mitosis
639 requires local disassembly of the nuclear envelope. *bioRxiv*, 779769 (2019).

640 67. A. Vještica, M. Marek, P. Nkosi, L. Merlini, G. Liu, M. Bérard, I. Billault-Chaumartin, S.

641 G. Martin, A toolbox of stable integration vectors in the fission yeast
642 *Schizosaccharomyces pombe*. *J. Cell Sci.* **133** (2020), doi:10.1242/jcs.240754.

643 68. J. Schindelin, I. Arganda-Carreras, E. Frise, V. Kaynig, M. Longair, T. Pietzsch, S.
644 Preibisch, C. Rueden, S. Saalfeld, B. Schmid, J. Y. Tinevez, D. J. White, V. Hartenstein,
645 K. Eliceiri, P. Tomancak, A. Cardona, Fiji: An open-source platform for biological-image
646 analysis. *Nat. Methods.* **9** (2012), pp. 676–682.

647 69. S. Berg, D. Kutra, T. Kroeger, C. N. Straehle, B. X. Kausler, C. Haubold, M. Schiegg, J.
648 Ales, T. Beier, M. Rudy, K. Eren, J. I. Cervantes, B. Xu, F. Beuttenmueller, A. Wolny, C.
649 Zhang, U. Koethe, F. A. Hamprecht, A. Kreshuk, ilastik: interactive machine learning
650 for (bio)image analysis. *Nat. Methods.* **16**, 1226–1232 (2019).

651 70. A. Halavaty, S. Terjung, in *Standard and Super-Resolution Bioimaging Data Analysis*
652 (John Wiley & Sons, Ltd, 2017), pp. 99–141.

653 71. W. J. H. Hagen, W. Wan, J. A. G. Briggs, Implementation of a cryo-electron
654 tomography tilt-scheme optimized for high resolution subtomogram averaging. *J.
655 Struct. Biol.* **197**, 191–198 (2017).

656 72. R. Danev, B. Buijsse, M. Khoshouei, J. M. Plitzko, W. Baumeister, Volta potential
657 phase plate for in-focus phase contrast transmission electron microscopy. *Proc. Natl.
658 Acad. Sci. U. S. A.* **111**, 15635–40 (2014).

659 73. D. N. Mastronarde, S. R. Held, Automated tilt series alignment and tomographic
660 reconstruction in IMOD. *J. Struct. Biol.* **197**, 102–113 (2017).

661 74. D. N. Mastronarde, Dual-Axis Tomography: An Approach with Alignment Methods
662 That Preserve Resolution. *J. Struct. Biol.* **120**, 343–352 (1997).

663 75. B. Turoňová, F. K. M. Schur, W. Wan, J. A. G. Briggs, Efficient 3D-CTF correction for
664 cryo-electron tomography using NovaCTF improves subtomogram averaging
665 resolution to 3.4 Å. *J. Struct. Biol.* **199**, 187–195 (2017).

666 76. B. Turoňová, M. Sikora, C. Schürmann, W. J. H. Hagen, S. Welsch, F. E. C. Blanc, S. von
667 Bülow, M. Gecht, K. Bagola, C. Hörner, G. van Zandbergen, S. Mosalaganti, A.
668 Schwarz, R. Covino, M. D. Mühlebach, G. Hummer, J. K. Locker, M. Beck, *bioRxiv*, in
669 press, doi:10.1101/2020.06.26.173476.

670 77. G. Tang, L. Peng, P. R. Baldwin, D. S. Mann, W. Jiang, I. Rees, S. J. Ludtke, EMAN2: An
671 extensible image processing suite for electron microscopy. *J. Struct. Biol.* **157**, 38–46
672 (2007).

673 78. B. Turoňová, W. J. H. Hagen, M. Obr, S. Mosalaganti, J. W. Beugelink, C. E. Zimmerli,
674 H. G. Kräusslich, M. Beck, Benchmarking tomographic acquisition schemes for high-
675 resolution structural biology. *Nat. Commun.* **11**, 1–9 (2020).

676 79. E. F. Pettersen, T. D. Goddard, C. C. Huang, G. S. Couch, D. M. Greenblatt, E. C. Meng,
677 T. E. Ferrin, UCSF Chimera - A visualization system for exploratory research and
678 analysis. *J. Comput. Chem.* **25**, 1605–1612 (2004).

679 80. L. Zimmermann, A. Stephens, S. Z. Nam, D. Rau, J. Kübler, M. Lozajic, F. Gabler, J.
680 Söding, A. N. Lupas, V. Alva, A Completely Reimplemented MPI Bioinformatics Toolkit
681 with a New HHpred Server at its Core. *J. Mol. Biol.* **430**, 2237–2243 (2018).

682 81. N. Guex, M. C. Peitsch, SWISS-MODEL and the Swiss-PdbViewer: An environment for
683 comparative protein modeling. *Electrophoresis.* **18**, 2714–2723 (1997).

684 82. A. Šali, T. L. Blundell, Comparative protein modelling by satisfaction of spatial
685 restraints. *J. Mol. Biol.* **234**, 779–815 (1993).

686 83. T. Stuwe, A. R. Correia, D. H. Lin, M. Paduch, V. T. Lu, A. A. Kossiakoff, A. Hoelz,
687 Architecture of the nuclear pore complex coat. *Science (80-).* **347**, 1148–1152
688 (2015).

689 84. D. H. Lin, T. Stuwe, S. Schilbach, E. J. Rundlet, T. Perriches, G. Mobbs, Y. Fan, K.
690 Thierbach, F. M. Huber, L. N. Collins, A. M. Davenport, Y. E. Jeon, A. Hoelz,
691 Architecture of the symmetric core of the nuclear pore. *Science (80-).* **352**, aaf1015–
692 aaf1015 (2016).

693 85. C. S. Weirich, J. P. Erzberger, J. M. Berger, K. Weis, The N-terminal domain of Nup159
694 forms a β -propeller that functions in mRNA export by tethering the helicase Dbp5 to
695 the nuclear pore. *Mol. Cell.* **16**, 749–760 (2004).

696 86. K. Yoshida, H. S. Seo, E. W. Debler, G. Blobel, A. Hoelz, Structural and functional
697 analysis of an essential nucleoporin heterotrimer on the cytoplasmic face of the
698 nuclear pore complex. *Proc. Natl. Acad. Sci. U. S. A.* **108**, 16571–16576 (2011).

699 87. K. Strimmer, fdrtool: A versatile R package for estimating local and tail area-based
700 false discovery rates. *Bioinformatics.* **24**, 1461–1462 (2008).

701 88. Y. Benjamini, Y. Hochberg, Controlling the false discovery rate: a practical and
702 powerful approach to multiple testing. *J. R. Stat. Soc. Ser. B.* **57**, 289–300 (1995).

703 89. T. D. Goddard, C. C. Huang, E. C. Meng, E. F. Pettersen, G. S. Couch, J. H. Morris, T. E.
704 Ferrin, UCSF ChimeraX: Meeting modern challenges in visualization and analysis.

705 *Protein Sci.* **27**, 14–25 (2018).

706 90. B. Webb, S. Viswanath, M. Bonomi, R. Pellarin, C. H. Greenberg, D. Saltzberg, A. Sali,
707 Integrative structure modeling with the Integrative Modeling Platform. *Protein Sci.*
708 **27**, 245–258 (2018).

709 91. D. Saltzberg, C. H. Greenberg, S. Viswanath, I. Chemmama, B. Webb, R. Pellarin, I.
710 Echeverria, A. Sali, in *Methods in Molecular Biology* (Humana Press Inc., 2019;
711 <https://pubmed.ncbi.nlm.nih.gov/31396911/>), vol. 2022, pp. 353–377.

712 92. G. Drin, J. F. Casella, R. Gautier, T. Boehmer, T. U. Schwartz, B. Antonny, A general
713 amphipathic α -helical motif for sensing membrane curvature. *Nat. Struct. Mol. Biol.*
714 **14**, 138–146 (2007).

715 93. H. Asakawa, H.-J. Yang, T. G. Yamamoto, C. Ohtsuki, Y. Chikashige, K. Sakata-Sogawa,
716 M. Tokunaga, M. Iwamoto, Y. Hiraoka, T. Haraguchi, Characterization of nuclear pore
717 complex components in fission yeast *Schizosaccharomyces pombe*. *Nucleus*. **5**, 149–
718 162 (2014).

719

720